energies

Article

Exploring Hydrogen–Diesel Dual Fuel Combustion in a Light-Duty Engine: A Numerical Investigation

Francesco Scrignoli [1,2], Alfredo Maria Pisapia [1], Tommaso Savioli [3], Ezio Mancaruso [4], Enrico Mattarelli [1,2] and Carlo Alberto Rinaldini [1,2,*]

[1] Dipartimento di Ingegneria "Enzo Ferrari", Università degli Studi di Modena e Reggio Emilia, Via Pietro Vivarelli 10, 41125 Modena, Italy; francesco.scrignoli@unimore.it (F.S.); alfredomaria.pisapia@unimore.it (A.M.P.); enrico.mattarelli@unimore.it (E.M.)
[2] InterMech—MO.RE., Via Pietro Vivarelli 2, 41125 Modena, Italy
[3] Atris Engineering s.r.l., Via Luigi Cherubini 5, 41122 Modena, Italy; tommaso.savioli@atrisengineering.it
[4] STEMS-CNR, Via Guglielmo Marconi 4, 80125 Napoli, Italy; ezio.mancaruso@stems.cnr.it
* Correspondence: carloalberto.rinaldini@unimore.it

Abstract: Dual fuel combustion has gained attention as a cost-effective solution for reducing the pollutant emissions of internal combustion engines. The typical approach is combining a conventional high-reactivity fossil fuel (diesel fuel) with a sustainable low-reactivity fuel, such as bio-methane, ethanol, or green hydrogen. The last one is particularly interesting, as in theory it produces only water and NO_x when it burns. However, integrating hydrogen into stock diesel engines is far from trivial due to a number of theoretical and practical challenges, mainly related to the control of combustion at different loads and speeds. The use of 3D-CFD simulation, supported by experimental data, appears to be the most effective way to address these issues. This study investigates the hydrogen-diesel dual fuel concept implemented with minimum modifications in a light-duty diesel engine (2.8 L, 4-cylinder, direct injection with common rail), considering two operating points representing typical partial and full load conditions for a light commercial vehicle or an industrial engine. The numerical analysis explores the effects of progressively replacing diesel fuel with hydrogen, up to 80% of the total energy input. The goal is to assess how this substitution affects engine performance and combustion characteristics. The results show that a moderate hydrogen substitution improves brake thermal efficiency, while higher substitution rates present quite a severe challenge. To address these issues, the diesel fuel injection strategy is optimized under dual fuel operation. The research findings are promising, but they also indicate that further investigations are needed at high hydrogen substitution rates in order to exploit the potential of the concept.

Keywords: dual fuel combustion; hydrogen; 3D-CFD simulation; fuel injection strategy

Citation: Scrignoli, F.; Pisapia, A.M.; Savioli, T.; Mancaruso, E.; Mattarelli, E.; Rinaldini, C.A. Exploring Hydrogen–Diesel Dual Fuel Combustion in a Light-Duty Engine: A Numerical Investigation. *Energies* **2024**, *17*, 5761. https://doi.org/10.3390/en17225761

Academic Editors: Vittorio Ravaglioli and Giacomo Silvagni

Received: 20 October 2024
Revised: 8 November 2024
Accepted: 13 November 2024
Published: 18 November 2024

1. Introduction

The environmental impact of fossil fuels burned by internal combustion engines (ICEs) has become a major concern in industrialized countries. Diesel engines, due to their high fuel efficiency and mechanical robustness, represent the mainstream technology for heavy-duty and industrial applications. However, compared to Spark Ignition (SI) gasoline engines, they emit significantly higher levels of nitrogen oxides (NO_x) and particulate matter (PM). These emissions are harmful for the environment and pose serious risks to human health [1–3]. As a result, NO_x and PM emissions have been heavily regulated, pushing manufacturers to implement more sophisticated and expensive after-treatment systems.

In order to face environmental regulations and the depletion of fossil fuel reserves, alternative fuels [4,5] and advanced combustion technologies [6,7] have been studied,

considering also the fuel production process [8–10]. These studies demonstrate benefits in terms of reduced emissions [11] and performance improvement [12,13].

Hydrogen (H_2) produced from renewable sources (often referred to as green H_2) has high potential to address many of the environmental challenges associated with traditional fossil fuels: the absence of CO_2 in the combustion products makes it very attractive for reducing greenhouse gas emissions and improving the overall environmental footprint of ICEs [14–16]. Nevertheless, implementing a H_2 combustion system into the current engine technologies presents several technical challenges.

In spark ignition (SI) engines, volumetric efficiency is reduced when the fuel is injected before intake valve closing. Due to its high flammability, even a small amount of H_2 rejected in the intake manifold may induce a backfire [17,18]; the risk of auto-ignition or knock is high for values of equivalence ratio > 0.5 [19–21]. Last but not least, the control of NO_x emissions requires ultra-lean mixtures, which are strongly penalizing for the engine power output [22].

H_2 can be used also in compression ignition (CI) engines, in conjunction with diesel fuel [23]: the latter is injected at the end of the compression stroke, in order to ignite a previously prepared lean mixture of H_2 and air. This hydrogen–diesel dual-fuel (H_2-D DF) concept leverages the benefits of hydrogen clean combustion while maintaining the cylinder design of a standard diesel engine (flat cylinder head, bowl in the piston, no spark plug). The advantages in terms of brake thermal efficiency and CO_2 and pollutant emissions are reported in several studies [24–26].

Unfortunately, the replacement of diesel fuel with hydrogen can lead to increased combustion temperatures, which may result in higher NO_x emissions and peak of pressure rise rate (PPRR), in comparison to the original diesel engine [27]. NOx and PPRR can be kept very low if an ultra-lean combustion is adopted, but the limits are the combustion stability and the cycle-by-cycle variation.

The support of three-dimensional computational fluid dynamics (3D-CFD) simulations, validated with experimental data, is essential to address the above-mentioned challenges [28]. Some experimental and numerical investigations reported in the literature have identified the diesel injection strategy [29], the substitution rate of H_2, and injection timing [30,31] as the key parameters for matching performance, thermal efficiency, and pollutant emissions.

An interesting aspect of H_2-D DF systems is the potential for retrofitting existing diesel engines and using a relatively small amount of H_2. This approach offers a practical and cost-effective solution for reducing the carbon footprint of current vehicles while awaiting a larger availability of green H_2 that will be possible only after the implementation of a capillary refueling infrastructure [32] and a reduction in H_2 production costs [33,34].

The goal of this article is to improve understanding of H_2-D DF combustion by means of a numerical investigation supported by experimental data, considering a typical light-duty diesel engine, which may be used for industrial applications and/or for light commercial vehicles. In particular, the influence of the H_2 substitution rate and of the diesel injection strategy is deeply analyzed, considering two fundamental operating conditions: medium load/medium speed (2400 rpm–10.5 bar BMEP) and high load/high speed (4000 rpm–13.5 bar BMEP).

2. Materials and Methods

2.1. Engine Characteristics

The engine selected for this study is a high-speed direct injection (HSDI) diesel engine manufactured by FCA–VM Motori in Cento (FE), Italy, and designed for automotive applications. It is a 4-cylinder in-line engine with a total displacement of 2780 cm^3, featuring four valves per cylinder. The engine is equipped with a high-pressure common rail fuel injection system and a set of six-hole injectors. Combustion chamber shape is highlighted in Figure 1. The bowl built inside the piston has a standard omega-shaped profile,

with a squish height of 0.9 mm and bowl volume of 32.8 cm^3. Other main characteristics of the engine are summarized in Table 1.

Figure 1. Cross section of a 60° sector of the combustion chamber, corresponding to one injector hole.

Table 1. Main features of the selected engine.

Engine Type	HSDI 4-Stroke Diesel, EURO IV
Cylinders	4 in-line
Total displacement (L)	2.78
Bore × Stroke (mm)	94 × 100
Connecting rod length (mm)	159
Compression ratio	17.5:1
Swirl ratio	1.8
N. of valves per cylinder	4
Exhaust valve opening (CA °AFTDC)	114
Intake valve opening (CA °AFTDC)	337
Exhaust valve closing (CA °AFTDC)	389
Intake valve closing (CA °AFTDC)	590
Air Metering	Turbocharger with VGT + Intercooler
Injection system	Common rail
Max. Injection press. (MPa)	160
Number of injector holes	6
Injector hole protrusion (mm)	2
Injector hole distance from injector axis (mm)	1.35
Injector hole diameter (mm)	0.153
Max. brake power (kW@rpm)	130@3800
Max. brake torque (Nm@rpm)	440@1750
Max. peak in-cylinder pressure (bar)	150
Max. Engine Speed (rpm)	4600

The above-mentioned engine was selected for this study due to its suitability for automotive application, making it an ideal candidate for exploring H_2-D DF combustion in this context. Furthermore, in previous research [35], the same engine was properly modified by the authors to operate in natural gas-diesel DF combustion, further demonstrating its appropriateness for the current study.

The baseline diesel engine was fully characterized at a steady dynamometer test bench, and two operating points with different engine speeds and brake mean effective pressures (BMEP) were considered for this study: a partial load condition (2400 rpm–10.5 bar BMEP) and a full load condition (4000 rpm–13.5 bar BMEP). These experimental conditions, which are summarized in Table 2, were used to validate the 3D-CFD model.

Table 2. Main engine parameters of the selected operating points.

	Partial Load	Full Load
Engine speed × BMEP (rpm × bar)	2400 × 10.5	4000 × 13.5
Brake Torque (Nm)	232	298
Brake Power (kW)	58.3	124.9
Diesel Fuel Mass (mg/cyl/cycle)	52.0	69.7
Injection strategy	pilot + pre + main	main

2.2. 3D-CFD Model Description and Validation

The numerical analysis described in this study was carried out by means of the AVL FIRE M 3D-CFD code, which is widely used in the automotive industry to simulate both cold flows and combustion processes in ICEs. The main models adopted for the simulations are summarized in Table 3. The Reynolds-averaged Navier–Stokes (RANS) approach was selected and the k-zeta-f model [36] was used to handle turbulence. The Kelvin-Helmholtz/Rayleigh-Taylor (KH–RT) [37] instability model was used for the diesel spray breakup modelling, whose gas phase is modeled with n-heptane (C_7H_{16}). Combustion was modeled thanks to the 3-Zones Extended Coherent Flame Model (ECFM-3Z) [38], which provides a good balance between accuracy and computational cost, in conjunction with the AVL database for laminar flame speeds.

Table 3. Main models used for 3D-CFD combustion modelling.

Equation of State	Real Gas/Peng-Robinson
Turbulence model	k-zeta-f
Wall treatment	Hybrid
Wall heat transfer model	Standard
Breakup model	Kelvin-Helmholtz/Rayleigh-Taylor
Wall interaction model	Kuhnke
Turbulent dispersion model	Solved
Drag model	Schiller-Naumann
Wall film model	Solved
Fuel evaporation model	Dukowicz
Diesel surrogate (gas phase)	C_7H_{16}
Combustion model	AVL ECFM-3Z
Auto ignition model	Two-Stage
Laminar flame speed	AVL database
Auto ignition delay	AVL database
NO_x model	Thermal mechanism

Both diesel and H_2-D DF simulations were carried out from intake valve closing (IVC) to exhaust valve opening (EVO), imposing a swirl ratio of 1.8, based on previous full engine cycle simulations. Therefore, thanks to the axial symmetry of the combustion chamber shape and the homogeneous spatial distribution of the six diesel injector holes, a 60° sector mesh was employed for the analysis (see Figure 2). The authors acknowledge the sector mesh approach approximates the real problem. In fact, the swirl axis may not be perfectly coincident with the cylinder axis and the geometric details of the head are missed. However, this simplification is acceptable, as it does not significantly impact the results of the analysis. The mesh also includes crevices (the gap between the piston skirt and the cylinder liner above the first ring), which were slightly increased to ensure that the compression ratio of the computational fluid domain matched the real one. The main characteristics of the mesh are summarized in Table 4.

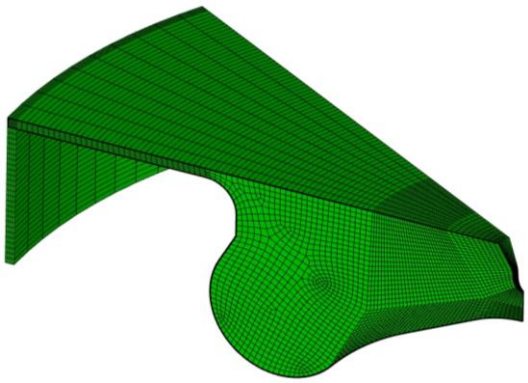

Figure 2. Computational grid at TDC.

Table 4. Main features of the computational grid.

Volume Cell Size (mm)	1.3 (0.65 from −30 to +30 °CA AFTDC)
Boundary layer thickness (mm)/n. of layers	0.1/2
Number of cells @ TDC	~ 70,000
Crevices: thickness × height (mm)	0.8 × 12.7

Both a mesh size and an angle-step (time-step) sensitivity analysis were conducted, during the injection/combustion process, to ensure that the numerical results were independent of the grid size and of the angle-step. For these analyses, the full load case (4000 rpm–13.5 bar BMEP) was considered.

First of all, three meshes with different average volume cell sizes were built: 1.3 mm, 0.65 mm, and 0.2 mm. Since the results from the last two meshes were in agreement, the 0.65 mm average-cell-size mesh was selected as the best compromise between accuracy and computational cost. The angle-step sensitivity analysis was performed considering three different values during the diesel fuel injection event: 0.01 °CA, 0.1 °CA, and 0.25 °CA. Since 0.1 °CA and 0.01 °CA angle steps guarantee almost the same peak in-cylinder pressure, 0.1 °CA was chosen with the aim to minimize the computational cost.

Outside of the injection phase, the time-step was set at the default values suggested by the software user's guide.

The 3D-CFD model was then validated against the selected diesel experimental data (2400 rpm–10.5 bar BMEP and 4000 rpm–13.5 bar BMEP), whose main engine parameters are listed in Table 5. Figure 3 shows the comparison between the measured and predicted in-cylinder pressure and apparent heat release rate (AHRR; Equation (1)), which are in good agreement. The main difference is represented by the underestimation of the maximum AHRR by the numerical model, both at partial and full load. The capability of the 3D-CFD model to correctly predict the combustion characteristics is confirmed by the comparison between the experimental and numerical results in terms of the gross indicated mean effective pressure (IMEP*; Equation (2)), peak in-cylinder pressure, and combustion phasing parameters reported in Tables 6 and 7.

Table 5. Diesel validation cases: main parameters for experiments and numerical simulations

Engine Parameters	2400 rpm–10.5 bar BMEP		4000 rpm–13.5 bar BMEP	
	Exp.	Num.	Exp.	Num.
Pressure @ IVC (bar)	2.5	2.5	1.5	1.5
Trapped mass (mg/cycle/cyl)	1283.5	1283.5	1640.2	1639.1
Diesel mass (mg/cycle/cyl)	52.00	52.00	69.70	69.60
Diesel SOI pilot (°CA AFTDC)	−14.7	−14.7	-	-
Diesel in pilot injection (mass%)	1.1	1.1	-	-
Diesel SOI pre (°CA AFTDC)	−0.6	−0.6	-	-
Diesel in pre injection (mass%)	2	2	-	-
Diesel SOI main (°CA AFTDC)	10.5	10.5	−12.0	−9.0

Diesel in main injection (mass%)	96.8	96.8	100.00	100.00
Residuals * (mass%)	7	7	5	5
EGR (mass%)	0	0	0	0
Swirl ratio (-)	1.8	1.8	1.8	1.8
Head temperature (K)	-	500	-	500
Liner temperature (K)	-	480	-	480
Piston temperature (K)	-	520	-	520

* based on the results of a validated GT-Power model of the full engine.

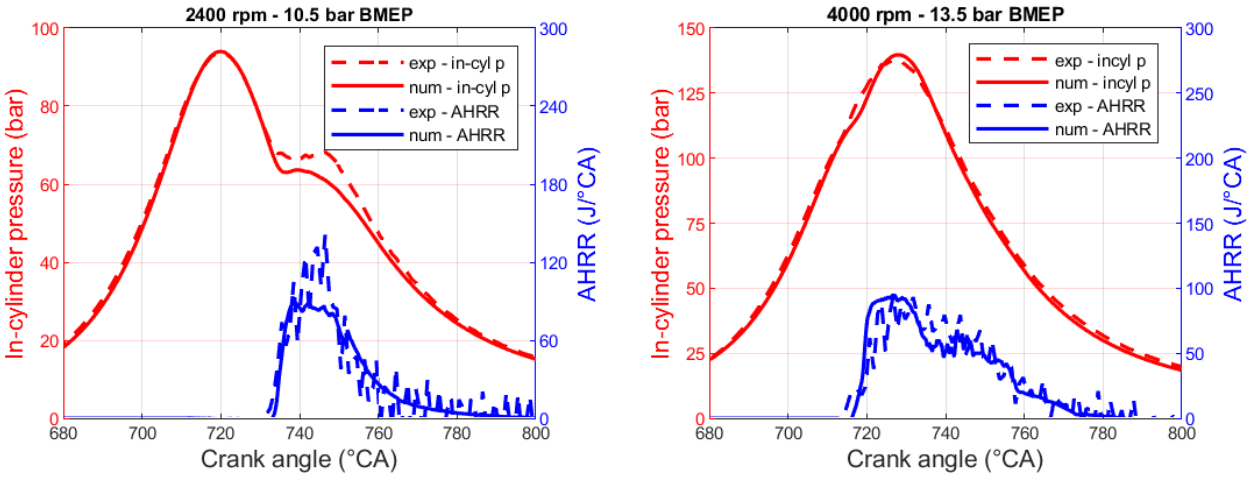

Figure 3. Comparison between experimental and numerical in-cylinder pressure and AHRR: (**a**) 2400 rpm–10.5 bar BMEP (**b**) 4000 rpm–13.5 bar BMEP.

$$\mathrm{AHRR} = \frac{\mathrm{k}}{\mathrm{k}-1}\mathrm{p}\frac{\mathrm{dV}}{\mathrm{d}\theta} + \frac{1}{\mathrm{k}-1}\mathrm{V}\frac{\mathrm{dp}}{\mathrm{d}\theta} \quad (1)$$

$$\mathrm{IMEP}^{*} = \frac{1}{V_d}\int_{\mathrm{IVC}}^{\mathrm{EVO}} \mathrm{pdV} \quad (2)$$

Table 6. Comparison between experimental and numerical IMEP*; peak in-cylinder pressure and combustion phasing parameters: 2400 rpm–10.5 bar BMEP.

Engine Parameter	Exp.	Num.	Absolute Error
IMEP* (bar)	11.30	10.61	0.69
Peak in-cylinder pressure (bar)	93.74	93.97	0.23
CA10 (°CA AFTDC)	17.5	17.8	0.3
CA50 (°CA AFTDC)	24.5	27.0	2.5
CA90 (°CA AFTDC)	38.5	43	4.5
Δθ10–90 (°CA)	21.0	25.2	4.2

Table 7. Comparison between experimental and numerical IMEP*; peak in-cylinder pressure and combustion phasing parameters: 4000 rpm–13.5 bar BMEP.

	Exp.	Num.	Absolute Error
IMEP* (bar)	21.70	21.25	0.27
Peak in-cylinder pressure (bar)	138.00	139.70	1.6
CA10 (°CA AFTDC)	2.8	2.9	-
CA50 (°CA AFTDC)	17.8	18.8	1
CA90 (°CA AFTDC)	42.8	46.0	3.2
Δθ10-90 (°CA)	40.0	43.1	3.1

It should be noted that the H_2-D DF experimental data of the selected engine are not yet available. Therefore, experimental data of a comparable diesel engine (Table 8), properly modified by the CNR-STEMS research center to operate in H_2-D DF combustion [39,40], were used to validate a 3D-CFD model of the latter engine. The new set of parameters was then used to update the numerical model of the VM engine. This approach ensured that the H_2-D DF combustion simulations for the VM engine were based on a reliable framework.

Table 8. Main features of the selected engine.

Engine Type	**4-stroke, Single Cylinder, Optically Accessible**
Stroke (mm)	92
Bore (mm)	85
Cylinder volume displacement (cm^3)	522
Combustion bowl volume (cm^3)	19.7
Compression ratio	16.5:1
Number of valves	4
EVO (CA °AFTDC)	116
IVO (CA °AFTDC)	344
EVC (CA °AFTDC)	380
IVC (CA °AFTDC)	588
Diesel injection system, common rail	
Number of holes	7
Cone angle of fuel jet axis (deg)	148
Hole diameter (mm)	0.141
Hydrogen PFI injection system	
Number of holes	1
Maximum injection pressure (bar)	5

Table 9 reports the main experimental data of the CNR-STEMS H_2-D DF engine and the comparison with the predictions of the corresponding 3D-CFD model, while Figure 4 illustrates the comparison between experimental and numerical in-cylinder pressure and AHRR. Once again, the simulation outcomes closely match the experimental measurements, demonstrating the robustness of the H_2-D DF combustion model.

Table 9. Comparison between experimental data and numerical results of the CNR-STEMS H_2-D DF single-cylinder research engine.

Engine Parameter	**Exp.**	**Num.**	**Absolute Error**
Engine speed (rpm)	2000		-
IMEP* (bar)	4.38	4.88	0.5
Experimental peak in-cylinder pressure (bar)	60.2	59.8	0.4
CA10 (°CA AFTDC)	–0.8	0.2	1
CA50 (°CA AFTDC)	9.4	9.6	0.2
CA90 (°CA AFTDC)	22.2	24.8	2.6
CA10-90 (°CA)	23	24.6	1.6

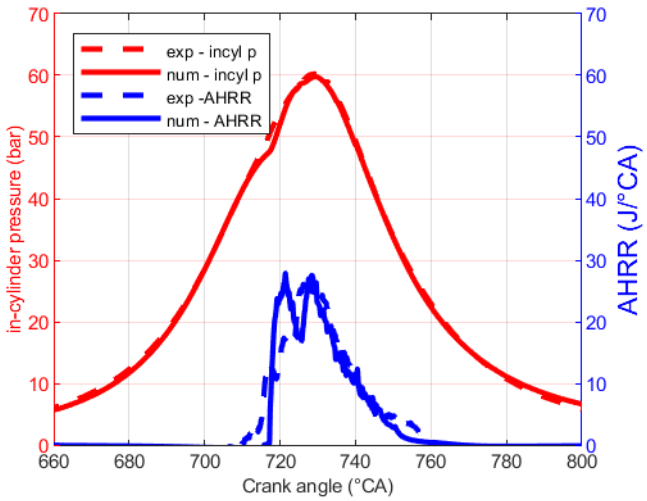

Figure 4. Comparison between experimental and numerical in-cylinder pressure and AHRR of the single-cylinder, optically accessible H_2-D DF engine.

2.3. Experimental Setup

The experimental investigations presented below were conducted using two distinct engine test benches located at different facilities: the engine test bench at the Department of Engineering "Enzo Ferrari" of the University of Modena and Reggio Emilia and the CNR-STEMS test bench. Both experimental campaigns were carried out to comprehensively evaluate the combustion characteristics and performance of the engines discussed in this work.

The first experimental setup was used to test the 2.8-liter turbocharged VM Motori (Cento (FE), Italy) diesel engine outlined in Table 1. Tests took place at the University of Modena and Reggio Emilia's engine test bench, equipped with an Apicom (Cento (FE), Italy) FR 400 BRV eddy-current dynamometer and Apicom (Cento (FE), Italy) Horus software for system control and data acquisition. Standard sensors for pressure and temperature monitoring were integrated, along with a Coriolis flow meter for precise diesel fuel consumption measurement. In-cylinder pressure traces were recorded using a high-frequency indicating system, which includes a Kistler piezoelectric, a charge amplifier, and an optical encoder. Data acquisition was conducted via a time-based method, with real-time analysis performed using Alma Automotive (Bologna, Italy) software on National Instruments (Austin, (USA)) Compact RIO hardware, achieving an angular resolution with a 0.3° crank angle.

The second setup employs an optical access single-cylinder compression ignition (CI) research engine (Table 8). The engine is equipped with a conventional extended piston, featuring a 46 mm flat sapphire window in the piston crown to enable visualization of the in-cylinder combustion process. A 45° visible-IR mirror within the extended piston reflects combustion images to high-speed cameras, capturing the entire combustion process. The engine maintains its original four-cylinder common rail injection system, controlled by an open electronic control unit (ECU) capable of adjusting injection timing, pressure, and duration. For premixed hydrogen injection, an electronic Port Fuel Injector (PFI) was installed in the intake manifold and connected to a compressed gas supply regulated at 5 bar. The premixed fuel was injected once the exhaust valves were closed to ensure effective mixing with intake air with no short-circuits. The ECU managed synchronization of the direct injection system, while a delay unit aligned the PFI timing with the engine cycle.

Additional features of this setup include the following:

- Air Flow and Pressure Monitoring: Intake air is conditioned (filtered, dehumidified, and temperature- and pressure-controlled) to maintain consistent in-cylinder conditions. The Sensyflow (Göttingen, Germany) FMT500-IG measures air mass flow rate.

- Gaseous Fuel Supply: The hydrogen supply line comprises a pressure regulator, flame arrester, and flame trapper. Gas flow rates are measured using a Brooks thermal mass flow meter.
- Data Acquisition: In-cylinder pressure is monitored using a piezoelectric transducer, and both the diesel and PFI injection signals are captured before it reaches the injector. Signals are digitized and recorded every 0.2° crank angle by means of a multichannel acquisition system. Pressure data from 200 combustion cycles are averaged, and heat release rates are calculated using thermodynamic principles.

2.4. Methodology

The updated VM engine numerical model was employed to investigate the effects of increasing H_2 energy fraction on engine performance, both at partial and full load (2400 rpm–10.5 bar BMEP and 4000 rpm–13.5 bar BMEP, respectively). In detail, simulations were conducted for H_2 energy shares of 20%, 40%, 60%, and 80% of the energy provided in the corresponding diesel operation. The progressive reduction in diesel fuel energy was produced by lowering the mass injected during the main injection (Figure 5) so as to guarantee a constant energy input for the specific operating point.

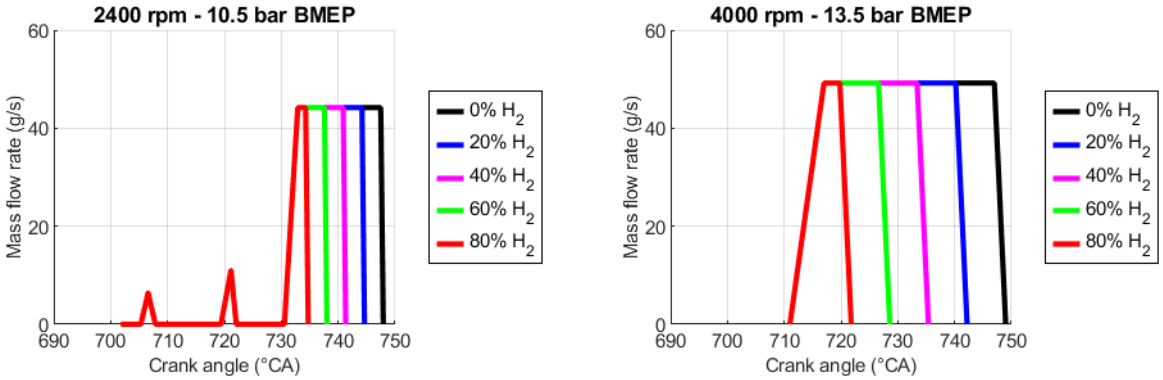

Figure 5. Diesel fuel injection strategy for diesel (black line) and H2-D DF operation with increasing H_2 energy share: (**a**) 2400 rpm–10.5 bar BMEP; (**b**) 4000 rpm–13.5 bar BMEP.

Experimentally, H_2 is responsible for a reduction in the volumetric efficiency of the engine when port injected. However, in the numerical investigation presented below, it was assumed that the total mass at IVC remains unchanged. This approach allows for simply considering the variation in H_2 content in the premixed charge, isolating the impact of H_2 substitution on the combustion process. It is important to highlight that the simulated condition can actually be achieved on the real engine by properly regulating the turbocharger.

Once the effects of increasing H_2 fraction on combustion characteristics were analyzed, a start of injection (SOI) sweep was carried out. This analysis was necessary because in DF combustion, as the substitution of diesel fuel with H_2 increases, the combustion shifts from being predominantly diffusion-based to predominantly premixed. Therefore, this requires optimization of the diesel fuel injection strategy. Furthermore, the simplicity of adjusting only the SOI makes this approach particularly well suited for achieving a straightforward and effective conversion, aligning with the objective of enabling dual-fuel conversion with minimal modifications.

The aim of these analyses is to recover the efficiency lost passing from diesel to DF combustion, potentially exceeding that of the corresponding diesel operation.

3. Results and Discussion

The results of the H_2-D DF combustion simulations, carried out with the VM engine numerical model, will be presented below. First, the partial load operating point will be discussed, followed by the full load condition.

3.1. Partial Load

Starting from the diesel operation at 2400 rpm–10.5 bar BMEP, corresponding to a partial load condition, H_2 energy share was progressively increased, passing from 0% (diesel combustion) to 80% of the energy provided with diesel fuel in diesel operation. The amount of diesel fuel is reduced accordingly, in order to keep the total energy input constant. Figure 6 shows the variation in the equivalence ratio of the H_2–air premixed charge (ϕ_{H_2}; Equation (3)) with increasing H_2 energy share.

$$\phi_{H_2} = \frac{\alpha_{s,H_2}}{\left(\frac{m_{a,TOT} - m_{a,D}}{m_{H_2}}\right)} \quad (3)$$

where ϕ_{H_2} is the equivalence ratio of the H_2-air premixed charge; α_{s,H_2} is the stoichiometric air to fuel ratio of H_2 (34.0); $m_{a,TOT}$ is the air mass trapped at IVC; $m_{a,D}$ is the air mass that reacts with diesel fuel, supposing diesel fuel combustion occurs in stoichiometric conditions; m_{H_2} is the H_2 mass trapped at IVC.

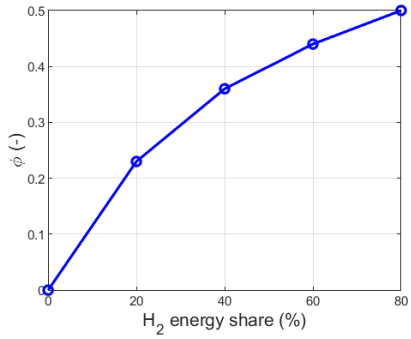

Figure 6. Variation in the equivalence ratio of the H_2-air premixed charge with increasing H_2 energy share at partial load (2400 rpm–10.5 bar BMEP).

Figures 7 and 8 report the effects of increasing H_2 mass fraction in the premixed charge on the in-cylinder pressure and rate of heat release (ROHR), peak in-cylinder pressure, peak pressure rise rate (PPRR), IMEP*, combustion efficiency (η_c), crank angles corresponding to 10, 50, and 90% of mass fraction burnt (CA10, CA50, CA90), and turbulent combustion duration (CA10–90). It should be noted that in the following discussion, ROHR will be used instead of AHRR, which represent, respectively, the total rate of heat released by the combustion process and the difference between the total rate of heat released during combustion and the wall heat flux.

As the H_2 energy content increases, the in-cylinder pressure at the end of the compression stroke, which corresponds to the peak in-cylinder pressure (Figure 8a), increases from about 94 to 98.7 bar. This is due to the higher γ (Equation (4)) of H_2 with respect to air.

$$\gamma = \frac{c_p}{c_v} \quad (4)$$

where c_p is the specific heat at constant pressure, while c_v is the specific heat at constant volume.

The PPRR appears slightly affected by the substitution of diesel fuel with H_2 since it increases by only 0.2 bar/°CA (from 2.9 to about 3.1 bar/°CA) passing from diesel combustion to 80% H_2-D DF combustion (Figure 8a). During combustion, the second peak in-

cylinder pressure increases until 60% of H_2 energy share, while a lowering of the second peak pressure appears at 80% of diesel fuel energy reduction. This depends on the combustion rate (ROHR), which speeds up until 60% of H_2 energy share then slows down. The reason is probably the progressive reduction in the diesel fuel mass, which, at 80% of energy substitution with H_2, constitutes a weak energy source to start combustion of the lean premixed charge.

IMEP* (Figure 8b) is positively affected by the substitution of the high-reactivity fuel with the low-reactivity one until 40% H_2 energy share, which produces an IMEP* improvement of 2.7% with respect to diesel combustion (from 10.6 to 10.9 bar). Higher energy substitutions result in worsening performance, with a maximum drop of 19.6% at 80% of H_2 energy share (from 10.6 to 8.5 bar). The IMEP* trend can be explained as follows: η_c continuously worsens as the H_2 energy share increases, with a maximum reduction of about 19.2% at 80% diesel fuel energy substitution (Figure 8b). This is probably due to the increase in ϕ_{H_2} and, consequently, of the premixed H_2 mass that cannot completely burn because of flame quenching near the combustion chamber walls and the mass of H_2 trapped in the crevices. However, combustion becomes faster up to 40% H_2 energy share, especially in the first part of the combustion process, as demonstrated by the shift of CA50 toward Top Dead Centre (TDC) (Figure 8c). Therefore, for low substitution, thermodynamic efficiency (η_{th}) increases, outweighing η_c effect. Then, CA10-90 (Figure 8d) increases significantly, and both η_{th} and η_c decrease, causing a deterioration in IMEP*.

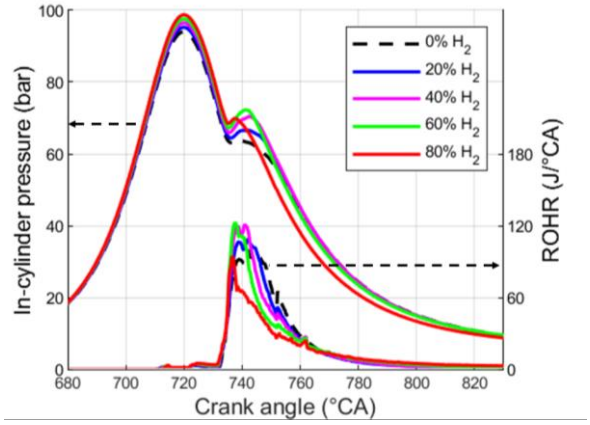

Figure 7. Effect of increasing H_2 energy share on in-cylinder pressure and ROHR at partial load (2400 rpm–10.5 bar BMEP).

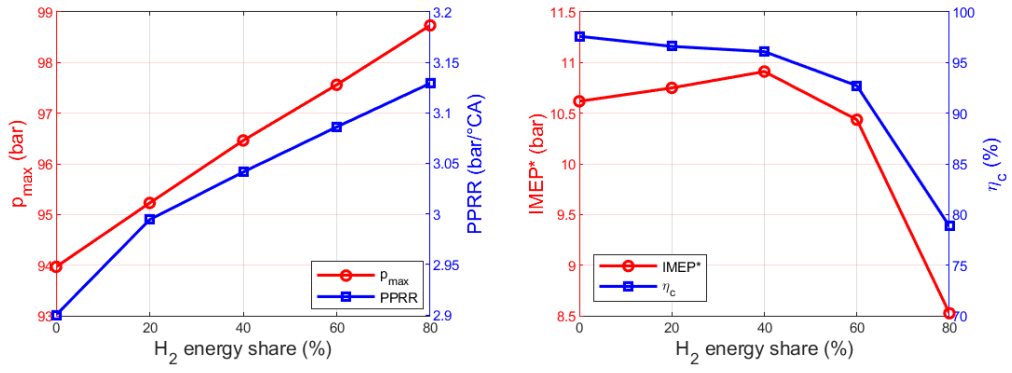

(**a**) (**b**)

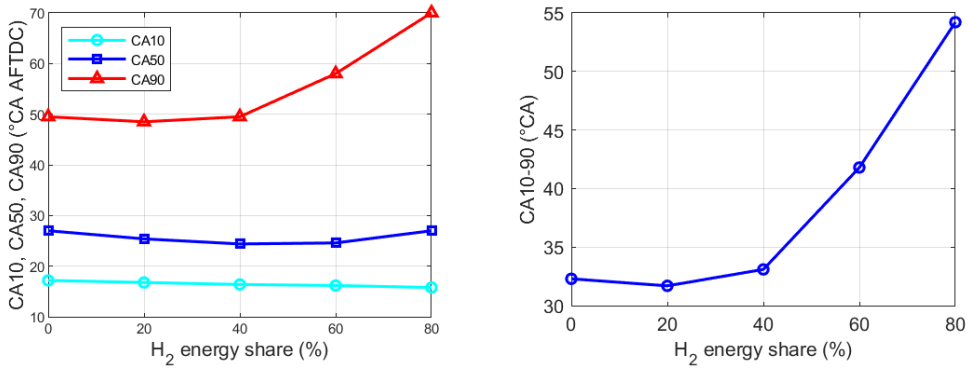

Figure 8. Effect of increasing H_2 energy share on the main combustion characteristics at partial load (2400 rpm–10.5 bar BMEP): (**a**) peak in-cylinder pressure and PPRR; (**b**) IMEP* and combustion efficiency; (**c**) combustion phasing parameters; (**d**) turbulent combustion duration.

In order to further improve performance in DF operation at low substitutions of diesel fuel with H_2 and to recover the efficiency lost at high substitutions, a design of experiment (DOE) was conducted by varying the SOI of the diesel fuel pilot and the pre and main injections. In particular, the diesel fuel injection strategies were rigidly shifted, advancing the SOI of the three injections from 5 to 30 °CA by steps of 5 °CA compared to the reference injection strategies (Figure 5a). As an example, Figure 9 shows the SOI variation applied to the diesel fuel injection strategy of the diesel case. As can be seen, the same SOI variation is applied to the three injections (pilot, pre, and main). The same approach was used for each of the H_2-D DF cases studied at partial load.

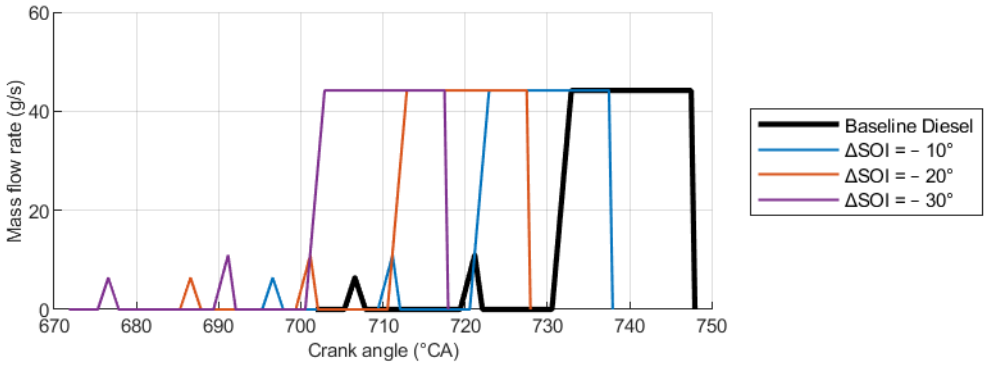

Figure 9. Effect of SOI variation on diesel fuel injection law for diesel case at partial load (2400 rpm–10.5 bar BMEP).

Figure 10 reports the contour maps of peak in-cylinder pressure, PPRR, IMEP*, and η_c as a function of H_2 energy share and SOI variation (ΔSOI). As can be seen from Figure 10c,d, the trends of IMEP* and η_c as a function of the H_2 energy share shown in Figure 8b are confirmed for all the ΔSOI values considered, except for the ΔSOI values of −25 and −30 °CA. For the latter ΔSOI values, IMEP* decreases with an increasing substitution of diesel fuel with H_2. Furthermore, IMEP* generally increases by advancing diesel fuel SOI. Therefore, IMEP* is maximized for small substitutions of diesel fuel with H_2 (20% H_2 energy share) and high diesel fuel injection advances (ΔSOI equal to −25 and −30 °CA), which correspond to an average improvement in IMEP* of about 27% compared to the reference diesel combustion.

However, two important constraints should be considered, namely, the maximum allowable in-cylinder pressure and PPRR. The following thresholds were imposed:

- maximum allowable in-cylinder pressure: 150 bar;

- maximum allowable PPRR: 5 bar/°CA.

The threshold on peak in-cylinder pressure corresponds to the maximum in-cylinder pressure compatible with the mechanical strength of the engine, while the PPRR limit was chosen in order to guarantee low levels of noise and vibrations, comparable to those of the reference diesel engine, that at the same operating point has PPRR= 2.9 bar/°CA. It can be observed that the constraint on PPRR is always stricter compared to the peak in-cylinder pressure constraint.

Based on the above considerations, the best compromise between performance improvement and limited mechanical stresses, noise, and vibrations can be achieved by advancing the diesel fuel injection strategies of the DF cases until reaching the PPRR = 5 bar/°CA limit.

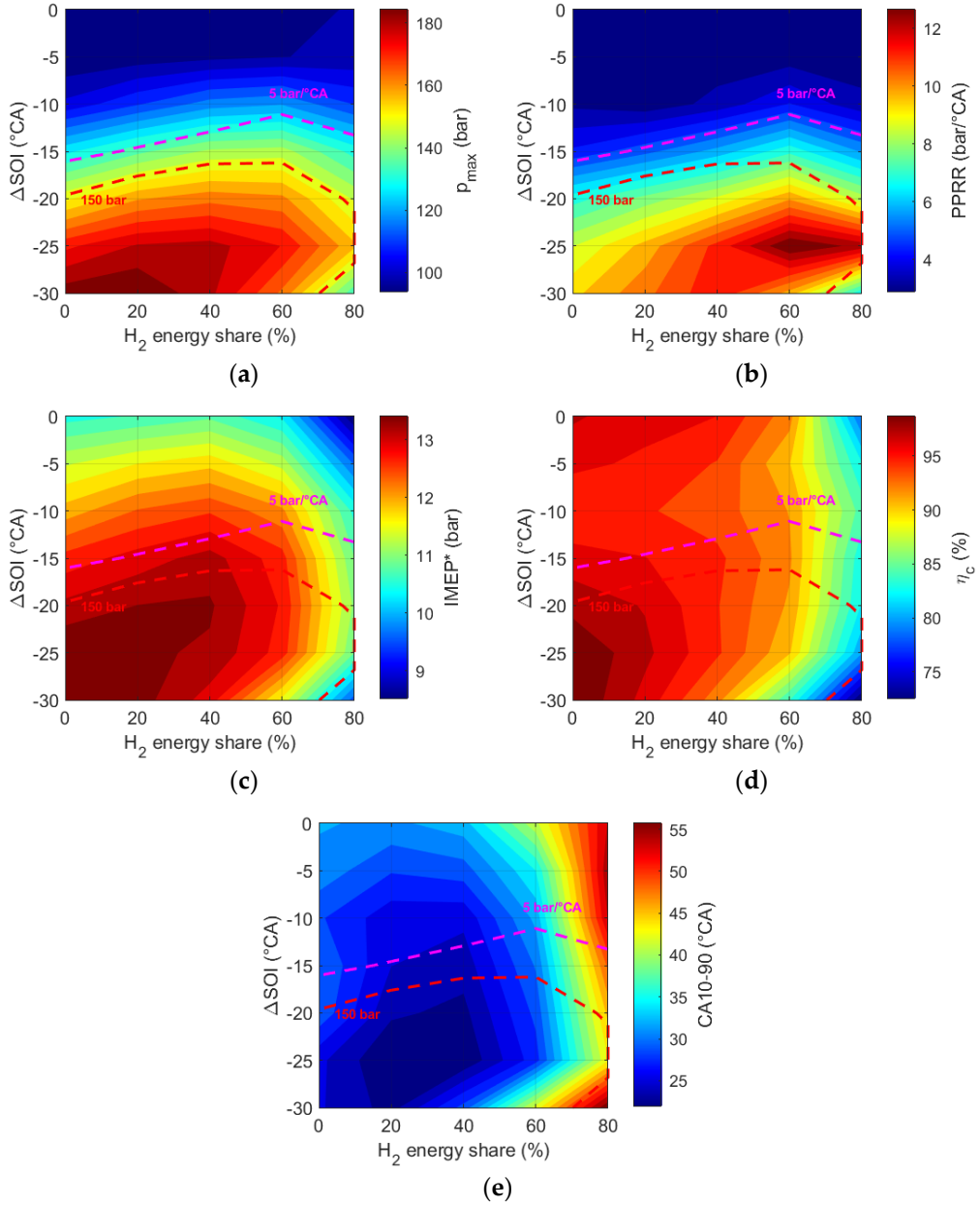

Figure 10. Influence of H2 energy share and diesel fuel SOI on main combustion characteristics at partial load (2400 rpm–10.5 bar BMEP): (**a**) peak in-cylinder pressure; (**b**) PPRR; (**c**) IMEP*; (**d**) combustion efficiency; (**e**) CA10-90.

Figure 11a depicts the diesel fuel SOI variations, with respect to the baseline diesel fuel injection strategies shown in Figure 5a, for the diesel and H_2-D DF cases that meet the PPRR limit of 5 bar/°CA. As can be seen, the ΔSOI must be gradually reduced as the H_2 energy share increases up to 60% and then starts increasing up to 80% H_2 energy share. As a result, peak in-cylinder pressure is always higher than in the baseline diesel and DF cases, but well below the above-mentioned threshold of 150 bar. As far as the combustion efficiency of the optimized cases is concerned (Figure 11b), it worsens as the H_2 mass fraction in the premixed charge increases. This is due to the increase in ϕ_{H_2} and, consequently, of the H_2 mass that cannot burn because of flame quenching near the combustion chamber walls and the mass of H_2 trapped in the crevices. Moreover, both optimized diesel and optimized H_2-D DF cases show lower combustion efficiency compared to the baseline diesel combustion, with the reduction ranging between 0.6% and 14%. However, the IMEP* of the optimized cases is always higher than in the baseline diesel case (IMEP* = 10.6 bar), with a maximum enhancement equal to + 22.9% at 40% H_2 energy share. This is due to the optimal combustion phasing produced by the diesel fuel SOI variation (advancement), which shifts CA50 toward TDC to about 10 °CA AFTDC, regardless of the H_2 energy share (Figure 11c). In addition, combustion duration reduces up to 40% H_2 energy share (Figure 11d). The above-mentioned effects overcome the reduction in η_c, enabling a relevant performance (IMEP*) improvement with respect to the baseline diesel case. At 60% H_2 energy share, combustion duration matches that of the baseline diesel case, while η_c further worsens it, reducing the IMEP* enhancement. Finally, if the maximum substitution of diesel fuel with H_2 is considered, both the drop in η_c and the significant increase in CA10-90 counteract the optimal combustion phasing, minimizing the IMEP* improvement with respect to the baseline diesel combustion.

It can therefore be concluded that, in DF operation at partial load, optimizing the diesel fuel SOI can improve engine performance. Advancing the diesel fuel injection timing significantly enhances performance at low H_2 energy shares, while at high H_2 substitution levels, it is possible to recover the drop in IMEP* caused by decreased combustion efficiency, even surpassing the IMEP* of the reference diesel case. However, η_c cannot be fully recovered by varying the SOI and remains lower than that of the reference diesel combustion.

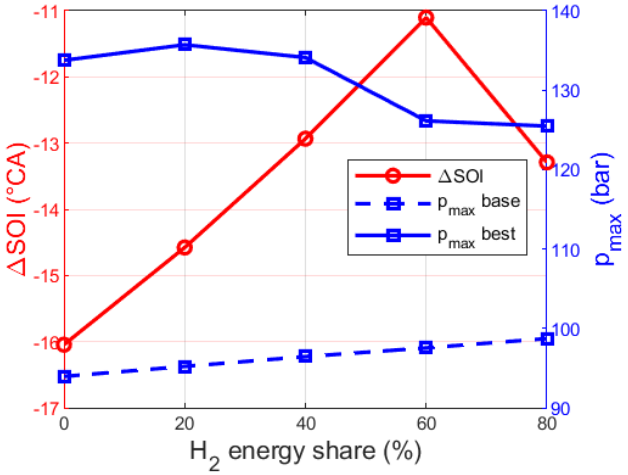

(**a**)

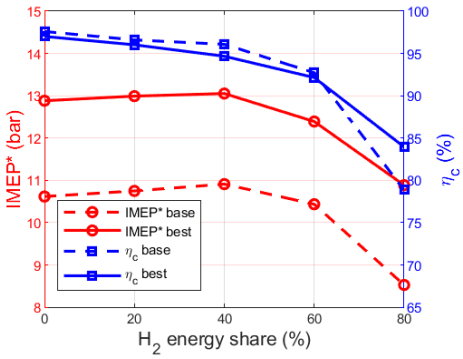

(**b**)

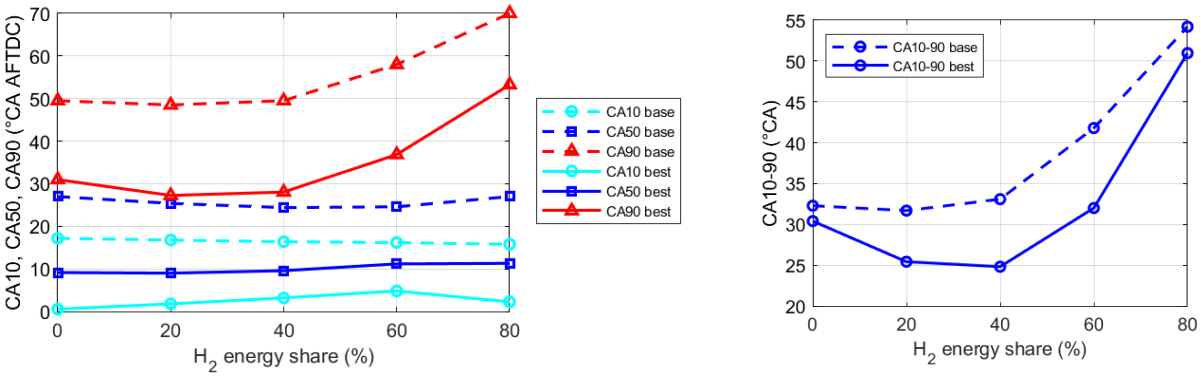

(**c**) (**d**)

Figure 11. Comparison among baseline diesel, optimized diesel, and optimized H_2-D DF cases in terms of the following: (**a**) peak in-cylinder pressure; (**b**) IMEP* and combustion efficiency; (**c**) combustion phasing; (**d**) combustion duration at partial load (2400 rpm–10.5 bar BMEP).

3.2. Full Load

The second condition that was investigated is the full load operating point: 4000 rpm–13.5 bar BMEP. Also, in this case, diesel fuel was progressively substituted with H_2, increasing the H_2 energy share from 0% to 80% of the energy provided with diesel fuel in the full load diesel operation. As in the partial load condition, the total energy input from the two fuels was kept constant, switching from diesel to DF combustion, and the diesel injection law was modified as shown in Figure 5b. Figure 12 shows ϕ_{H_2} of the premixed H_2-air charge, as defined in Equation (3), as a function of the H_2 energy share.

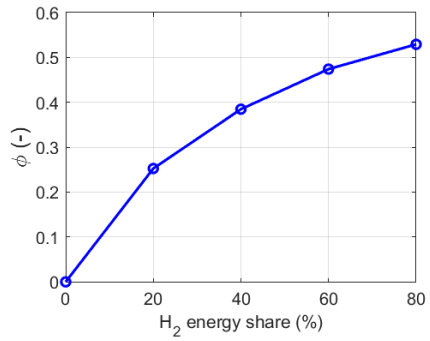

Figure 12. Variation in the equivalence ratio of the H_2-air premixed charge with increasing H_2 energy share at full load (4000 rpm–13.5 bar BMEP).

The introduction of H_2 leads to a significant increase in peak in-cylinder pressure, which rises from 139.7 bar in the diesel operation to 182.3 bar when 80% of energy is supplied by H_2 (Figures 13 and 14a). This trend aligns with similar studies that demonstrate the effects of H_2 on pressure rise in DF engines at medium-high loads [41]. Peak in-cylinder pressure rise is due to the intensification of the ROHR as the amount of H_2 increases. In fact, passing from diesel to DF H_2-D combustion, the combustion process transitions from diffusive to premixed. Moreover, H_2 is characterized by a laminar flame speed higher than any other fuel and the widest flammability range. It is also interesting to notice that the ignition delay increases with the H_2 energy fraction. This effect is attributable to two causes: in order to guarantee the same mass at IVC as the H_2 fraction increases, temperature at IVC must be reduced, which decreases temperature at the end of the compression stroke; H_2 tends to absorb part of the heat released by diesel fuel during the low temperature heat release, delaying the start of the high temperature heat release.

As far as combustion phasing is concerned (Figure 14c), CA10 is almost unaffected by variation in the H_2 energy share, while CA50 is always decreasing with growing H_2

energy share (from 18.8 °CA AFTDC to 9.2 °CA AFTDC), in accordance with the intensification of the ROHR. CA90 initially decreases, reaching its lowest point at 40% H_2 energy share, then increases. As a result, CA10-90 shortens up to 40% H_2 energy share (CA10-90 = 33 °CA AFTDC; −10 °CA with respect to diesel operation), then turbulent combustion slows down due to the increasing amount of the premixed charge located in the periphery of the combustion chamber that burns slowly and partially (Figure 14d).

IMEP* increases as the H_2 fraction rises, peaking at 60% H_2 energy share (23.1 bar; + 9.0% compared to diesel combustion), as depicted in Figure 14b. However, η_c decreases with increasing H_2 substitution until 40% H_2 energy share (92.2%; −1.7% compared to diesel combustion), then starts to increase, reaching a value comparable to that of diesel combustion at 80% H_2 energy share.

Therefore, the trend of IMEP* can be attributed to the faster combustion rate observed with higher H_2 fractions and demonstrated by the shift of CA50 toward TDC (Figure 14c), which leads to a greater η_{th} that is capable of outweighing the η_c worsening.

However, it should be noted that the maximum allowable peak in-cylinder pressure for the VM engine is 150 bar (Table 1), while the peak in-cylinder pressure in DF operation at full load is always higher than the above-mentioned limit. Moreover, PPRR rises with the mass fraction of H_2 in the premixed charge, reaching almost 19 bar/°CA (Figure 14a).

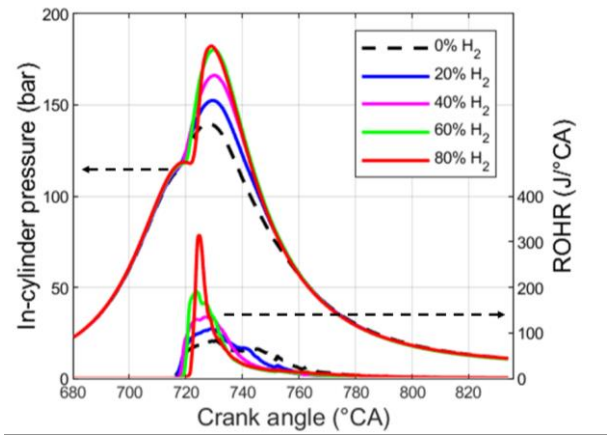

Figure 13. Effect of increasing H_2 energy share on in-cylinder pressure and ROHR at full load (4000 rpm–13.5 bar BMEP).

Therefore, it is essential to optimize the diesel fuel injection strategy with the aim to achieve efficient DF combustion with acceptable mechanical stresses, noise, and vibrations.

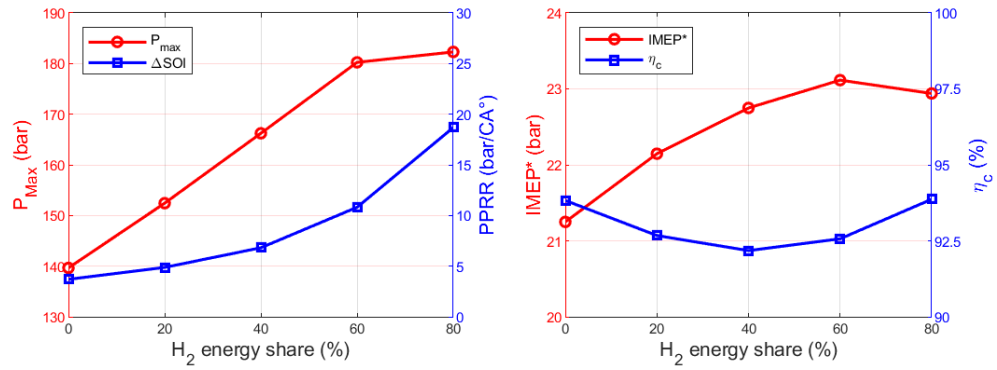

(**a**) (**b**)

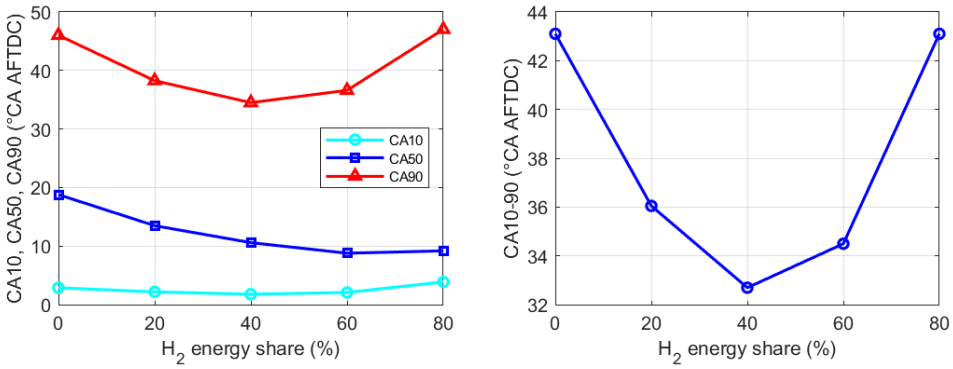

Figure 14. Effect of increasing H_2 energy share on main combustion characteristics at full load (4000 rpm–13.5 bar BMEP): (**a**) peak in-cylinder pressure and PPRR; (**b**) IMEP* and combustion efficiency; (**c**) combustion phasing parameters; (**d**) turbulent combustion duration.

In detail, a DOE was performed, varying SOI of the diesel fuel main injection by an angle between −3 °CA and + 6 °CA by steps of 1 °CA, with respect to the baseline diesel fuel injection strategy. In Figure 15, the effect of the SOI variation on the injection strategy of the diesel case is illustrated. As can be seen, the main injection timing was shifted both forward and backward. The same SOI variation was applied to each of the H_2-D DF cases studied. Linear interpolation was applied to estimate the results for the SOI and H_2 energy share values not directly simulated.

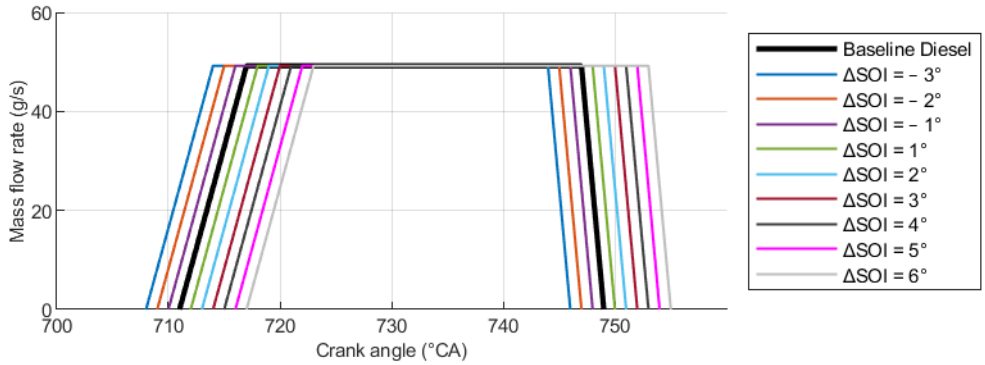

Figure 15. Effect of SOI variation on diesel fuel injection law for diesel case at full load (4000 rpm–13.5 bar BMEP).

Figure 16 reports the contour maps of peak in-cylinder pressure, PPRR, IMEP*, and η_c. Three lines are also drawn on the maps: the red dashed line represents the maximum allowable peak in-cylinder pressure of the VM engine (150 bar); the red dotted line corresponds to the maximum in-cylinder pressure of the baseline diesel engine (140 bar); and the magenta dashed line is the acceptable limit on PPRR based on the engine application (12 bar/°CA).

Figure 16a confirms the peak in-cylinder pressure trend with H_2 energy share observed for the baseline diesel fuel injection strategy, showing that this trend is observable for all the SOI values considered. It also highlights that the baseline diesel engine operates with some margin, as the peak pressure of 140 bar remains below the maximum allowable limit. This indicates the possibility of advancing the injection timing by approximately 2 °CA without surpassing structural constraints. It is noteworthy that the peak pressure limit is more restrictive than the PPRR constraint. However, unlike the partial load condition, where both limits produced nearly parallel curves on the maps, the behavior here is different. Specifically, while both H_2 substitution and injection timing advance have a similar influence on the peak pressure (with limit curves inclined at approximately 45°), the

impact of H_2 substitution on PPRR seems to be more pronounced, resulting in nearly vertical limit curves. Unlike partial load conditions, where H_2 can be substituted across all studied fractions by adjusting the SOI, at full load it is not possible to exceed 78.4% H_2 energy share if the ΔSOI is restricted to a maximum value of 6 °CA. This limitation in H_2 energy share arises due to the PPRR constraint.

From Figure 16c, it appears that IMEP* is more influenced by the H_2 energy share than the diesel fuel SOI and increases as the diesel fuel SOI is advanced and ϕ_{H_2} is increased. For the baseline full diesel configuration, advancing the fuel injection by 2 °CA results in a 0.8% increase in IMEP* a reduction of 1.9% in η_c. The figure also shows that η_c is maximized for ΔSOI values between +3 °CA and +6 °CA and for H_2 energy share values below 20%, while advancing the diesel fuel SOI compared to the injection strategy of the reference diesel case is generally disadvantageous.

The IMEP* trend with H_2 energy share and ΔSOI, despite the behavior of η_c, suggests that the overall engine efficiency improves due to the faster combustion associated with the increasing ϕ_{H_2} of the premixed charge. In confirmation of this, Figure 16e reports the contour map of CA10-90, which is minimum for negative ΔSOI values and H_2 energy shares between 20% and 60%.

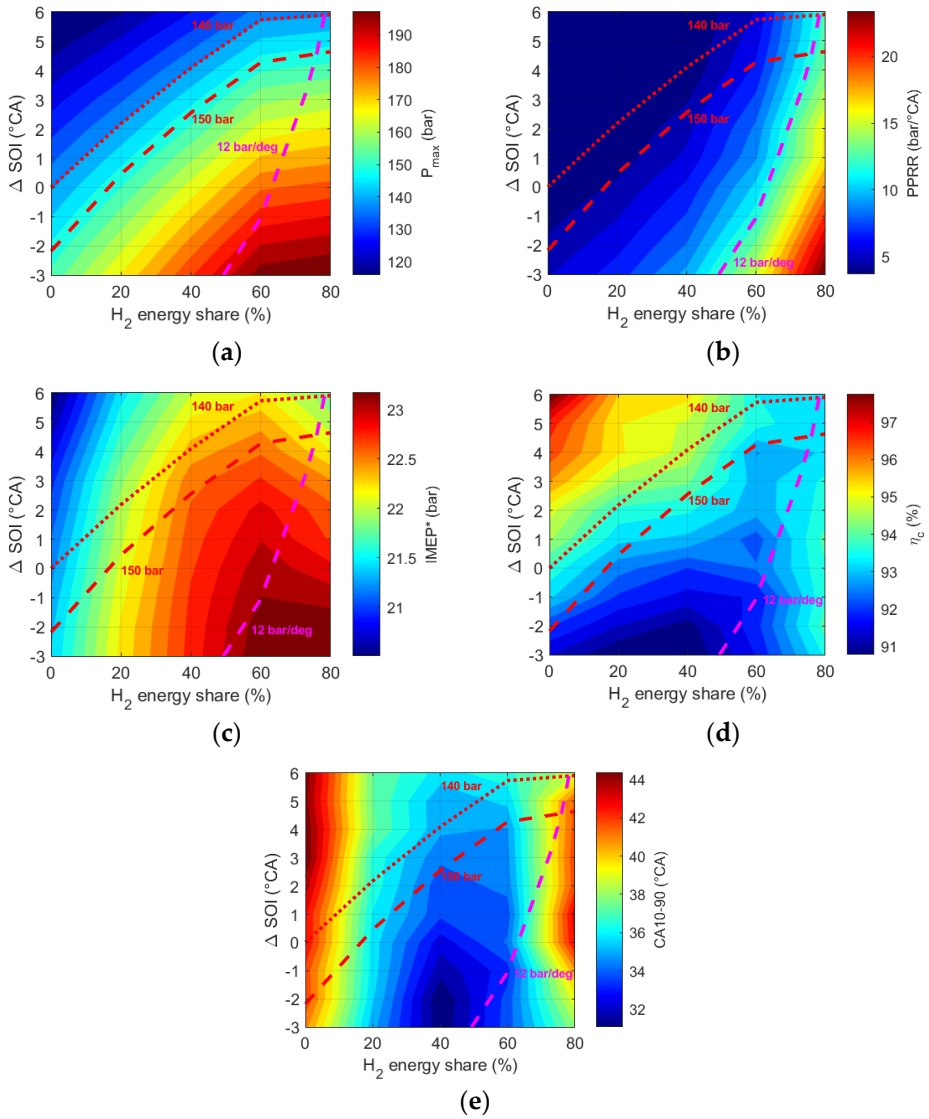

Figure 16. Influence of H_2 energy share and diesel fuel SOI on main combustion characteristics at full load (4000 rpm–13.5 bar BMEP): (**a**) peak in-cylinder pressure; (**b**) PPRR; (**c**) IMEP*; (**d**) combustion efficiency; (**e**) CA10-90.

Based on the previous analysis, the SOI value that permitted us to maximize the IMEP* in full diesel and DF operations was selected for each H_2 energy share, considering also the constraints on peak in-cylinder pressure (150 bar) and PPRR (12 bar/°CA). Figure 17 highlights that ΔSOI should be progressively delayed as the H_2 mass fraction increases in order to achieve the above-mentioned targets for peak in-cylinder pressure and PPRR. Additionally, the figure shows that in the baseline DF case the SOI was not modified; for this reason, the engine exceeded its structural limits.

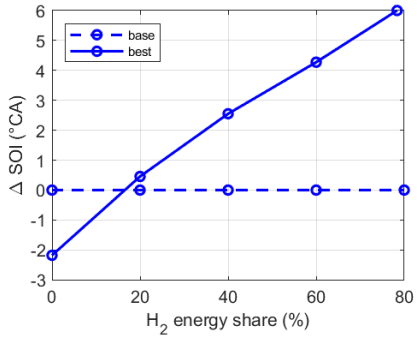

Figure 17. SOI comparison between baseline and optimized (best) diesel fuel injection strategy for different H_2 energy shares.

DF cases with optimized ΔSOI are compared with the DF cases with the baseline injection strategy in terms of peak in-cylinder pressure, PPRR, IMEP*, η_c, combustion phasing parameters, and combustion duration (Figure 18).

It can be observed that by optimizing the injection timing of the baseline diesel engine with ΔSOI= −2.2 °CA, a gain of 0.2 bar in BMEP (0.8%) is achieved but results in a reduction of 1.9% in efficiency, as previously mentioned. Figure 18a confirms that the SOI optimization keeps the peak pressure and PPRR within structural limits. Notably, in Figure 18b, all dual fuel configurations employing the optimized injection strategy show higher IMEP* values compared to both the baseline diesel configuration and the diesel engine with optimized injection timing. However, regarding combustion ηc, only the configuration with a 40% H_2 share surpasses the performance of the two full diesel configurations. This 40% H_2 share case, with its optimized injection law (ΔSOI = 2.55 °CA), achieves the highest IMEP* and combustion efficiency among all the optimized cases. Specifically, it increases IMEP* by 1.2 bar (5.6%) and combustion efficiency by 2.1% compared to the optimized diesel case.

Figure 18c,d display the characteristic combustion timing. It can be observed that hydrogen substitution consistently accelerates combustion compared to the diesel case. Figure 18d shows that, even for the optimized cases, the minimum combustion duration is achieved at a 40% H_2 share. For higher hydrogen shares, the combustion duration tends to increase as the hydrogen moves more toward the periphery and farther from the injection zone, slowing down the combustion process.

An additional notable point is observed at the maximum admissible hydrogen energy substitution corresponding to 78.4%. In this case, ΔSOI is set to the maximum value of 6 °CA (Figure 17), IMEP* increases by 0.47 bar (2.2%), and combustion efficiency improves by 1.3% compared to the optimized full diesel case. These results demonstrate that H_2 can effectively substitute diesel while maintaining engine performance, in some cases even improving it, with respect to the baseline engine configuration and while keeping the engine in safe working condition.

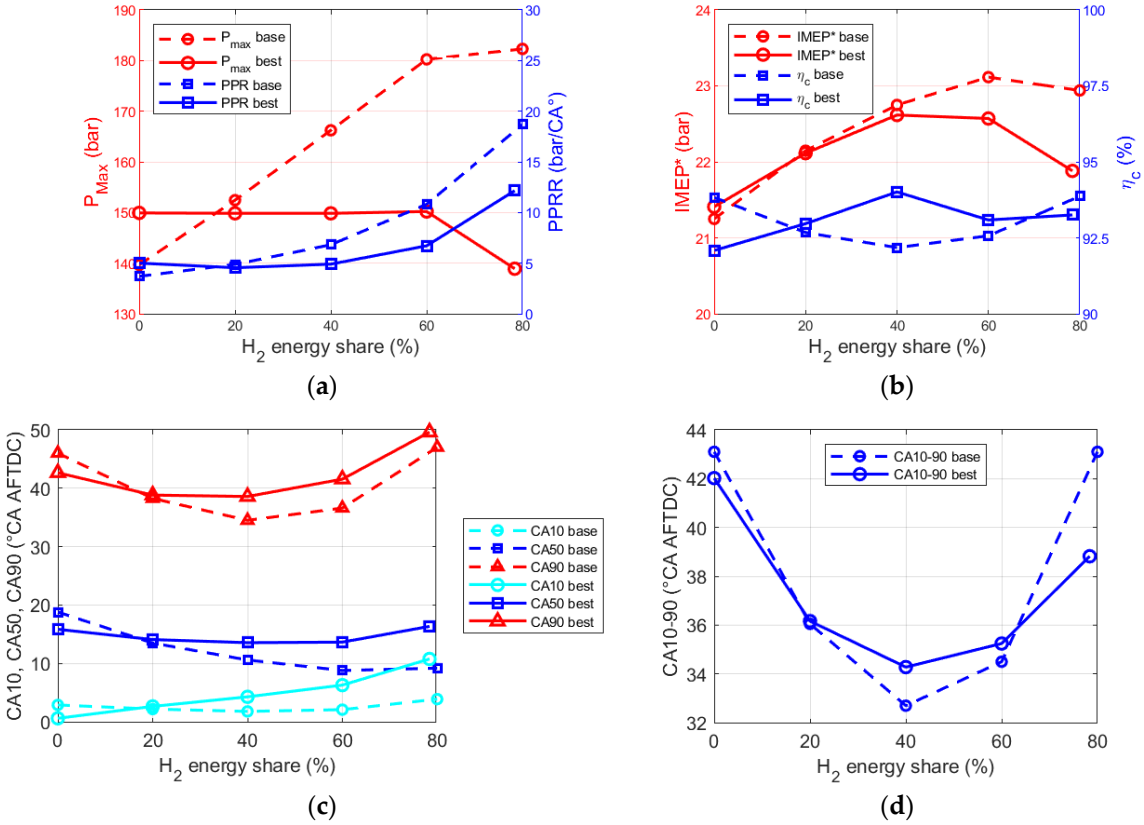

Figure 18. Comparison between the main combustion characteristics before and after the diesel fuel SOI optimization at full load (4000 rpm–13.5 bar BMEP): (**a**) peak in-cylinder pressure and PPRR; (**b**) IMEP* and combustion efficiency; (**c**) combustion phasing parameters; (**d**) turbulent combustion duration.

Finally, the two most relevant operating points were selected and analysed in comparison with the baseline diesel case. The selected points are as follows: the 78.4% H_2-D DF case with ΔSOI = 6°, as it represents the highest hydrogen share, and the 40% H_2-D DF case with ΔSOI = 2.55°, as it achieved the highest IMEP. Figure 19 compares the baseline diesel engine (red dashed line) with the two DF cases with optimized ΔSOI (green and blue lines) in terms of pressure trace and ROHR. The figure shows that the 40% H_2 case reaches the highest peak pressure at 150 bar, compared to 139.7 bar for the baseline diesel and 138.9 bar for the 78.4% H_2 case (which is very close to baseline diesel peak pressure). The highest PPRR is obtained in the 78.4% H_2 case, hitting the structural limit as a result of the optimization process. Most significantly, Figure 19 shows that the pressure trends are significantly different across the cases, with the most distinctive pattern observed in the case with the highest H_2 energy share. This case is characterized by a notable double-peak in the pressure curve with a very sharp ROHR trace.

In terms of IMEP*, Table 10 shows that the 40% H_2 H_2-D DF case has a gain of 1.36 bar (+6.40%) compared to the baseline diesel (the gain is 1.20 bar (+5.60%) compared to the optimized diesel), while the 78.4% H_2 H_2-D DF case has a lower gain of 0.63 bar (+2.96%) compared to the baseline diesel (the gain is 0.47 bar (+2.20%) compared to the optimized diesel). η_c increases by 0.2% for the 40% H_2 share and decreases by 0.6% for the 78.4% H_2 case. Finally, combustion duration is reduced by 8.8 °CA for the 40% H_2 share and by 4.3 °CA for the 78.4% H_2 share, when compared to the diesel baseline.

From both the general analysis conducted earlier and the examination of these specific operating points, it can be concluded that, at full load, the transition from diesel to H_2-D DF operation invariably requires modifications to the injection timing strategy to maintain mechanical stresses within acceptable thresholds. Furthermore, optimal engine

performance, characterized by a significant increase in IMEP* compared to the pure diesel case, is achieved at intermediate H_2 substitution levels (approximately 40%). At higher H_2 shares, the combustion process becomes more abrupt, and the necessary delay in injection timing, required to limit peak in-cylinder pressure and the PPRR, negatively impacts the cycle efficiency, leading to performance levels that struggle to reach those of the reference diesel case.

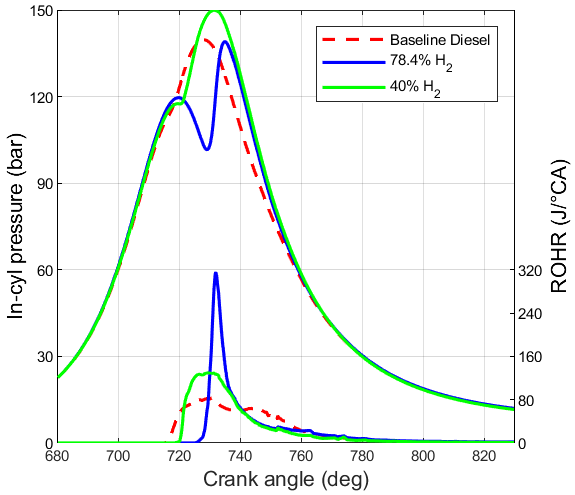

Figure 19. Comparison between baseline diesel operation and optimized 80% H_2-D DF combustion at full load (4000 rpm–13.5 bar BMEP) in terms of in-cylinder pressure and ROHR.

Table 10. Comparison between diesel and optimized 80% H2-D DF.

	Diesel	Opt. Diesel	40% H_2 H_2-D DF	78% H_2 H_2-D DF
H_2 energy share (%)	0	0	40	80
ΔSOI (°CA)	0	−2.18	−2.55	−6.00
Max in-cylinder pressure (bar)	139.7	150.0	150.0	138.9
PPRR (bar/°CA)	3.71	5.01	4.91	12.00
IMEP* (bar)	21.25	21.41	22.61	21.88
η_c (%)	93.82	92.09	94.01	93.25
CA10-90 (°CA)	43.1	42.0	34.3	38.8

4. Conclusions

This numerical study investigated the implementation of hydrogen-diesel dual fuel (H_2-D DF) combustion in a light-duty diesel engine, focusing on the effects of increasing H_2 substitution for diesel fuel and on the optimization of the diesel fuel injection strategy. Two operating points were analyzed: a medium load/medium speed (2400 rpm–10.5 bar BMEP) condition and a high load/high speed (4000 rpm–13.5 bar BMEP) condition.

For the first partial load point, based on the analysis presented in this paper, the following conclusions can be drawn:

- Increasing the H_2 energy share up to 40% improves IMEP* thanks to the faster combustion process. Higher energy substitutions determine a reduction in IMEP*, which was observed to drop at 80% H_2 energy share;
- The performance deterioration at high H_2 substitutions is due to the worsening of the combustion efficiency, which reduces as the H_2 mass fraction in the premixed charge increases;
- Advancing the diesel fuel injection strategy of the DF cases further improves performance at low H_2 energy shares, while at high H_2 substitutions it is possible to recover

the drop in IMEP*, exceeding the IMEP* of the baseline diesel case. However, combustion efficiency cannot be recovered by advancing the diesel fuel SOI, which remains lower than that of the baseline diesel combustion.

- Under full load conditions, the following observations were made:
- H_2 leads to significant increases in both peak in-cylinder pressure and pressure rise rate (PPRR), exceeding the engine's structural limits. To mitigate these effects and ensure safe operation, a delay in diesel injection is necessary. In this analysis, an optimal SOI was determined for each H_2 energy share to keep the peak pressure and PPRR within acceptable limits.
- Optimal IMEP* is achieved at around 40% hydrogen substitution; however, higher levels lead to abrupt combustion and reduced efficiency, resulting in performance that falls short of the diesel baseline.
- Two optimal points were then identified: configuration with 40% H_2 energy share and ΔSOI = 2.55° CA (maximizes IMEP*, achieving a 6.4% increase compared to the baseline diesel engine and obtains the highest combustion efficiency); configuration with 78.4% H_2 energy share and ΔSOI = 6° CA (permits the maximum H_2 share and achieves a 2.96% increase in IMEP* compared to the baseline diesel engine, with a slight reduction in combustion efficiency).

These findings demonstrate that injection timing optimization plays a critical role in enabling the conversion of diesel engines to dual fuel operation, enhancing performance while respecting the engine's structural limits. The conversion of conventional diesel engines to H_2-DF systems is not only feasible in terms of performance but it can also be essential for the future of sustainable transportation. However, several technological challenges remain, including H_2 injection technology, material compatibility, regulatory frameworks, and infrastructure development.

Author Contributions: Conceptualization, F.S., A.M.P., T.S., E.M. (Ezio Mancaruso), E.M. (Enrico Mattarelli), and C.A.R.; methodology, F.S., A.M.P., T.S., E.M. (Ezio Mancaruso), E.M. (Enrico Mattarelli), and C.A.R.; software, F.S., A.M.P., T.S., E.M. (Ezio Mancaruso), E.M. (Enrico Mattarelli), and C.A.R.; validation, F.S., A.M.P., T.S., E.M. (Ezio Mancaruso), E.M. (Enrico Mattarelli), and C.A.R.; formal analysis, F.S., A.M.P., T.S., E.M. (Ezio Mancaruso), E.M. (Enrico Mattarelli), and C.A.R.; investigation, F.S., A.M.P., T.S., E.M. (Ezio Mancaruso), E.M. (Enrico Mattarelli), and C.A.R.; resources, F.S., A.M.P., T.S., E.M. (Ezio Mancaruso), E.M. (Enrico Mattarelli), and C.A.R.; data curation, F.S., A.M.P., T.S., E.M. (Ezio Mancaruso), E.M. (Enrico Mattarelli), and C.A.R.; writing—original draft preparation, F.S., A.M.P., T.S., E.M. (Ezio Mancaruso), E.M. (Enrico Mattarelli), and C.A.R.; writing—review and editing, F.S., A.M.P., T.S., E.M. (Ezio Mancaruso), E.M. (Enrico Mattarelli), and C.A.R.; visualization, F.S., A.M.P., T.S., E.M. (Ezio Mancaruso), E.M. (Enrico Mattarelli), and C.A.R.; supervision, F.S., A.M.P., T.S., E.M. (Ezio Mancaruso), E.M. (Enrico Mattarelli), and C.A.R. All authors have read and agreed to the published version of the manuscript.

Funding: This research received no external funding.

Data Availability Statement: The datasets presented in this article are not readily available because the data are part of an ongoing study. Requests to access the datasets should be directed to the corresponding author.

Acknowledgments: AVL Italia Srl and AVL List GmbH are gratefully acknowledged for the FIRE M R2023.2 license granted to the University of Modena and Reggio Emilia.

Conflicts of Interest: The authors declare no conflicts of interest.

Abbreviations

ICE	Internal Combustion Engine	ECFM	Extended Coherent Flame Model
PM	Particulate Matter	EVO	Exhaust Valve Opening
SI	Spark Ignition	IVO	Intake Valve Opening
CI	Compression Ignition	EVC	Exhaust Valve Closing
H_2-D DF	Hydrogen-Diesel Dual Fuel	IVC	Intake Valve Closing
PPRR	Peak Pressure Rise Rate	SOI	Start Of Injection

3D-CFD	Three-Dimensional Computational Fluid Dynamic	AHRR	Apparent Heat Release Rate
HSDI	High Speed Direct Injection	ROHR	Rate Of Heat Release
BMEP	Brake Mean Effective Pressure	MFB	Mass Fuel Burned
IMEP*	gross Indicated Mean Effective Pressure	CA10	Crank Angle corresponding to MFB10
°CA	Crank Angle degrees	CA50	Crank Angle corresponding to MFB50
TDC	Top Dead Center	CA90	Crank Angle corresponding to MFB90
AFTDC	After Firing Top Dead Center	EGR	Exhaust Gas Recirculation
RANS	Reynolds-Averaged Navier-Stokes	DOE	Design Of Experiment

Chemical formulae

NO_x	Nitrogen Oxides
H_2	Hydrogen
CO_2	Carbon dioxide
C_7H_{16}	n-Heptane

Symbols

ϕ	Equivalence ratio
α	Air to fuel ratio
α_s	Stoichiometric air to fuel ratio
m	Mass
γ	Specific heat at constant pressure to specific heat at constant volume ratio
η	Efficiency
Δ	Variation

References

1. Ge, C.; Peters, S.; Olsson, A.; Portengen, L.; Schüz, J.; Almansa, J.; Ahrens, W.; Bencko, V.; Benhamou, S.; Boffetta, P.; et al. Diesel Engine Exhaust Exposure, Smoking, and Lung Cancer Subtype Risks. A Pooled Exposure–Response Analysis of 14 Case–Control Studies. *Am. J. Respir. Crit. Care Med.* **2020**, *202*, 402–411. https://doi.org/10.1164/rccm.201911-2101OC.
2. Long, E.; Carlsten, C. Controlled Human Exposure to Diesel Exhaust: Results Illuminate Health Effects of Traffic-Related Air Pollution and Inform Future Directions. *Part. Fibre Toxicol.* **2022**, *19*, 11. https://doi.org/10.1186/s12989-022-00450-5.
3. Burnett, R.; Chen, H.; Szyszkowicz, M.; Fann, N.; Hubbell, B.; Pope, C.A.; Apte, J.S.; Brauer, M.; Cohen, A.; Weichenthal, S.; et al. Global Estimates of Mortality Associated with Long-Term Exposure to Outdoor Fine Particulate Matter. *Proc. Natl. Acad. Sci. USA* **2018**, *115*, 9592–9597. https://doi.org/10.1073/pnas.1803222115.
4. Stančin, H.; Mikulčić, H.; Wang, X.; Duić, N. A Review on Alternative Fuels in Future Energy System. *Renew. Sustain. Energy Rev.* **2020**, *128*, 109927. https://doi.org/10.1016/j.rser.2020.109927.
5. Balamurugan, T.; Arun, A.; Sathishkumar, G.B. Biodiesel Derived from Corn Oil—A Fuel Substitute for Diesel. *Renew. Sustain. Energy Rev.* **2018**, *94*, 772–778. https://doi.org/10.1016/j.rser.2018.06.048.
6. Shim, E.; Park, H.; Bae, C. Comparisons of Advanced Combustion Technologies (HCCI, PCCI, and Dual-Fuel PCCI) on Engine Performance and Emission Characteristics in a Heavy-Duty Diesel Engine. *Fuel* **2020**, *262*, 116436. https://doi.org/10.1016/j.fuel.2019.116436.
7. Rinaldini, C.A.; Scrignoli, F.; Savioli, T.; Mattarelli, E. Combustion Optimization of a Premixed Ultra-Lean Blend of Natural Gas and Hydrogen in a Dual Fuel Engine Running at Low Load. *SAE Int. J. Engines* **2023**, *17*, 03–17-04–0025. https://doi.org/10.4271/03-17-04-0025.
8. Uzoejinwa, B.B.; He, X.; Wang, S.; El-Fatah Abomohra, A.; Hu, Y.; Wang, Q. Co-Pyrolysis of Biomass and Waste Plastics as a Thermochemical Conversion Technology for High-Grade Biofuel Production: Recent Progress and Future Directions Elsewhere Worldwide. *Energy Convers. Manag.* **2018**, *163*, 468–492. https://doi.org/10.1016/j.enconman.2018.02.004.
9. Alvarez, J.; Kumagai, S.; Wu, C.; Yoshioka, T.; Bilbao, J.; Olazar, M.; Williams, P.T. Hydrogen Production from Biomass and Plastic Mixtures by Pyrolysis-Gasification. *Int. J. Hydrog. Energy* **2014**, *39*, 10883–10891. https://doi.org/10.1016/j.ijhydene.2014.04.189.
10. Deka, T.J.; Osman, A.I.; Baruah, D.C.; Rooney, D.W. Methanol Fuel Production, Utilization, and Techno-Economy: A Review. *Environ. Chem. Lett.* **2022**, *20*, 3525–3554. https://doi.org/10.1007/s10311-022-01485-y.
11. Park, Y.; Moses-DeBusk, M.; Sluder, S.S.; Huff, S.P. Impact of Biofuel Blending on Hydrocarbon Speciation and Particulate Matter from a Medium-Duty Multimode Combustion Strategy. *Energies* **2023**, *16*, 5735. https://doi.org/10.3390/en16155735.
12. Hartikka, T.; Kuronen, M.; Kiiski, U. Technical Performance of HVO (Hydrotreated Vegetable Oil) in Diesel Engines. *SAE Tech. Pap.* **2012**, 2012–01–1585. https://doi.org/10.4271/2012-01-1585

13. Masuk, N.I.; Mostakim, K.; Kanka, S.D. Performance and Emission Characteristic Analysis of a Gasoline Engine Utilizing Different Types of Alternative Fuels: A Comprehensive Review. *Energy Fuels* **2021**, *35*, 4644–4669. https://doi.org/10.1021/acs.energyfuels.0c04112.
14. Singh, S.; Jain, S.; Ps, V.; Tiwari, A.K.; Nouni, M.R.; Pandey, J.K.; Goel, S. Hydrogen: A Sustainable Fuel for Future of the Transport Sector. *Renew. Sustain. Energy Rev.* **2015**, *51*, 623–633. https://doi.org/10.1016/j.rser.2015.06.040.
15. De Boer, P.C.T.; McLean, W.J.; Homan, H.S. Performance and Emissions of Hydrogen Fueled Internal Combustion Engines. *Int. J. Hydrog. Energy* **1976**, *1*, 153–172. https://doi.org/10.1016/0360-3199(76)90068-9.
16. Stępień, Z. A Comprehensive Overview of Hydrogen-Fueled Internal Combustion Engines: Achievements and Future Challenges. *Energies* **2021**, *14*, 6504. https://doi.org/10.3390/en14206504.
17. Gao, J.; Wang, X.; Song, P.; Tian, G.; Ma, C. Review of the Backfire Occurrences and Control Strategies for Port Hydrogen Injection Internal Combustion Engines. *Fuel* **2022**, *307*, 121553. https://doi.org/10.1016/j.fuel.2021.121553.
18. Khalid, A.H.; Muhamad Said, M.F.; Veza, I.; Abas, M.A.; Roslan, M.F.; Abubakar, S.; Jalal, M.R. Hydrogen Port Fuel Injection: Review of Fuel Injection Control Strategies to Mitigate Backfire in Internal Combustion Engine Fuelled with Hydrogen. *Int. J. Hydrog. Energy* **2024**, *66*, 571–581. https://doi.org/10.1016/j.ijhydene.2024.04.087.
19. Li, H. Knock in Spark Ignition Hydrogen Engines. *Int. J. Hydrog. Energy* **2004**, *29*, 859–865. https://doi.org/10.1016/j.ijhydene.2003.09.013.
20. Moradi, R.; Groth, K.M. Hydrogen Storage and Delivery: Review of the State of the Art Technologies and Risk and Reliability Analysis. *Int. J. Hydrog. Energy* **2019**, *44*, 12254–12269. https://doi.org/10.1016/j.ijhydene.2019.03.041.
21. Crowl, D.A.; Jo, Y.-D. The Hazards and Risks of Hydrogen. *J. Loss Prev. Process Ind.* **2007**, *20*, 158–164. https://doi.org/10.1016/j.jlp.2007.02.002.
22. Kahraman, E.; Cihangir Ozcanlı, S.; Ozerdem, B. An Experimental Study on Performance and Emission Characteristics of a Hydrogen Fuelled Spark Ignition Engine. *Int. J. Hydrog. Energy* **2007**, *32*, 2066–2072. https://doi.org/10.1016/j.ijhydene.2006.08.023.
23. Hosseini, S.H.; Tsolakis, A.; Alagumalai, A.; Mahian, O.; Lam, S.S.; Pan, J.; Peng, W.; Tabatabaei, M.; Aghbashlo, M. Use of Hydrogen in Dual-Fuel Diesel Engines. *Progress. Energy Combust. Sci.* **2023**, *98*, 101100. https://doi.org/10.1016/j.pecs.2023.101100.
24. Karagöz, Y.; Sandalcı, T.; Yüksek, L.; Dalkılıç, A.S.; Wongwises, S. Effect of Hydrogen–Diesel Dual-Fuel Usage on Performance, Emissions and Diesel Combustion in Diesel Engines. *Adv. Mech. Eng.* **2016**, *8*, 168781401666445. https://doi.org/10.1177/1687814016664458.
25. Castro, N.; Toledo, M.; Amador, G. An Experimental Investigation of the Performance and Emissions of a Hydrogen-Diesel Dual Fuel Compression Ignition Internal Combustion Engine. *Appl. Therm. Eng.* **2019**, *156*, 660–667. https://doi.org/10.1016/j.applthermaleng.2019.04.078.
26. Nag, S.; Sharma, P.; Gupta, A.; Dhar, A. Experimental Study of Engine Performance and Emissions for Hydrogen Diesel Dual Fuel Engine with Exhaust Gas Recirculation. *Int. J. Hydrog. Energy* **2019**, *44*, 12163–12175. https://doi.org/10.1016/j.ijhydene.2019.03.120.
27. Luo, Q.; Hu, J.-B.; Sun, B.; Liu, F.; Wang, X.; Li, C.; Bao, L. Experimental Investigation of Combustion Characteristics and NOx Emission of a Turbocharged Hydrogen Internal Combustion Engine. *Int. J. Hydrog. Energy* **2019**, *44*, 5573–5584. https://doi.org/10.1016/j.ijhydene.2018.08.184.
28. Mancaruso, E.; Catapano, F.; Rossetti, S.; Anaclerio, G.; Camporeale, S.; Episcopo, D.; Laera, D.; Torresi, M. *High Pressure Hydrogen Injector Sizing Using 1D/3D CFD Modeling for a Compression Ignition Single Cylinder Research Engine*; Detroit, MI, USA, 2024; *SAE Technical paper* 2024–01–2615; https://doi.org/10.4271/2024-01-2615
29. Tripathi, G.; Sharma, P.; Dhar, A.; Sadiki, A. Computational Investigation of Diesel Injection Strategies in Hydrogen-Diesel Dual Fuel Engine. *Sustain. Energy Technol. Assess.* **2019**, *36*, 100543. https://doi.org/10.1016/j.seta.2019.100543.
30. Saravanan, N.; Nagarajan, G. Experimental Investigation on a DI Dual Fuel Engine with Hydrogen Injection. *Int. J. Energy Res.* **2009**, *33*, 295–308. https://doi.org/10.1002/er.1477.
31. Mancaruso, E.; Rossetti, S.; Vaglieco, B.M. *Analysis of Dual Fuel Hydrogen/Diesel Combustion Varying Diesel and Hydrogen Injection Parameters in a Single Cylinder Research Engine*; Detroit, MI, USA, 2024; *SAE Technical paper* 2024–01–2363; https://doi.org/10.4271/2024-01-2363
32. Alazemi, J.; Andrews, J. Automotive Hydrogen Fuelling Stations: An International Review. *Renew. Sustain. Energy Rev.* **2015**, *48*, 483–499. https://doi.org/10.1016/j.rser.2015.03.085.
33. Sinigaglia, T.; Lewiski, F.; Santos Martins, M.E.; Mairesse Siluk, J.C. Production, Storage, Fuel Stations of Hydrogen and Its Utilization in Automotive Applications-a Review. *Int. J. Hydrog. Energy* **2017**, *42*, 24597–24611. https://doi.org/10.1016/j.ijhydene.2017.08.063.
34. El-Emam, R.S.; Özcan, H. Comprehensive Review on the Techno-Economics of Sustainable Large-Scale Clean Hydrogen Production. *J. Clean. Prod.* **2019**, *220*, 593–609. https://doi.org/10.1016/j.jclepro.2019.01.309.
35. Mattarelli, E.; Rinaldini, C.A.; Savioli, T.; Scrignoli, F. Optimization of a High-Speed Dual-Fuel (Natural Gas-Diesel) Compression Ignition Engine for Gen-Sets. *SAE Int. J. Engines* **2021**, *14*, 03–14-03–0022. https://doi.org/10.4271/03-14-03-0022.
36. Hanjalić, K.; Popovac, M.; Hadžiabdić, M. A Robust Near-Wall Elliptic-Relaxation Eddy-Viscosity Turbulence Model for CFD. *Int. J. Heat. Fluid. Flow.* **2004**, *25*, 1047–1051. https://doi.org/10.1016/j.ijheatfluidflow.2004.07.005.
37. Beale, J.C.; Reitz, R.D. Modeling Spray Atomization with the Kelvin-Helmholtz/Rayleigh-Taylor Hybrid Model. *Atomization and Sprays* **1999**, *9*, 623–650. https://doi.org/10.1615/AtomizSpr.v9.i6.40.

38. Colin, O.; Benkenida, A. The 3-Zones Extended Coherent Flame Model (Ecfm3z) for Computing Premixed/Diffusion Combustion. *Oil Gas. Sci. Technol.—Rev. IFP* **2004**, *59*, 593–609. https://doi.org/10.2516/ogst:2004043.
39. Mancaruso, E.; De Robbio, R.; Vaglieco, B.M. Hydrogen/Diesel Combustion Analysis in a Single Cylinder Research Engine. *SAE Int. J. Adv. Curr. Prac. Mobil.* **2022**, *5*, 1312–1321. https://doi.org/10.4271/2022-24-0012.
40. Mancaruso, E.; Rossetti, S.; Vaglieco, B.M.; De Robbio, R.; Maroteaux, F. *Optical Diagnostics to Study Hydrogen/Diesel Combustion with EGR in a Single Cylinder Research Engine*; Capri, Italy, 2023; SAE Techical paper 2023–24–0070; https://doi.org/10.4271/2023-24-0070.
41. Rahnama, P.; Paykani, A.; Reitz, R.D. A Numerical Study of the Effects of Using Hydrogen, Reformer Gas and Nitrogen on Combustion, Emissions and Load Limits of a Heavy Duty Natural Gas/Diesel RCCI Engine. *Appl. Energy* **2017**, *193*, 182–198. https://doi.org/10.1016/j.apenergy.2017.02.023.